General formulation of coupled radiative and conductive heat transfer between compact bodies

Weiliang Jin, Riccardo Messina, Alejandro W. Rodriguez

General formulation of coupled radiative and conductive heat transfer between compact bodies

Weiliang Jin,[1] Riccardo Messina,[2] and Alejandro W. Rodriguez[1]

[1]*Department of Electrical Engineering, Princeton University, Princeton, NJ 08544, USA*
[2]*Laboratoire Charles Coulomb, Université de Montpellier and CNRS, Montpellier, France*

We present a general framework for studying strongly coupled radiative and conductive heat transfer between arbitrarily shaped bodies separated by sub-wavelength distances. Our formulation is based on a macroscopic approach that couples our recent fluctuating volume–current (FVC) method of near-field heat transfer to the more well known Fourier conduction transport equation, in which case the former can induce temperature gradients throughout the bodies. Although the FVC framework can in principle be applied to arbitrary geometries, in practice it is most applicable in situations where only one of the bodies undergoes significant temperature gradients. To illustrate the capabilities of this framework, we consider an idealized, proof-of-concept geometry involving two aluminum-zinc oxide nanorods separated by a vacuum gap, with one of the rods heated by a large-temperature reservoir one one side while the other is held at room temperature. We show that the presence of bulk nanorod polaritonic resonances can result in very large radiative heat transfer rates (roughly five times larger than what is achievable in the planar configuration) and leads to nonlinear temperature profiles.

Radiative heat transfer (RHT) between objects held at different temperatures can be many orders of magnitude larger in the near field (short separations $d \ll$ thermal wavelength $\lambda_T = \hbar c/k_{\rm B}T$) than for far-away objects [1–5]. Recently, we showed that that the interplay of near-field RHT and conduction in planar geometries can dramatically modify the temperature and thermal exchange rate at sub-micron separations [6, 7]. Such strongly-coupled conduction–radiation (CR) phenomena are bound to play a larger role in situations involving structured materials, where RHT can be further enhanced [8–13] and modified [14–17], and in on-going experiments exploring nanometer scale gaps, where the boundary between conductive (phonon- and electron-mediated) and radiative transport begins to blurr [18, 19].

We present a general CR framework that captures the interplay of near-field RHT and thermal conduction along with the existence of large temperature gradients in arbitrary geometries. We show that under certain conditions, i.e. materials and structures with separations and geometric lengthscales in the nanometer range, RHT can approach and even exceed conduction, significantly changing the stationary temperature distribution of heated objects. Our approach is based on a generalization of our recent fluctuating volume-current (FVC) formulation of electromagnetic (EM) fluctuations, which when coupled to the more standard Fourier heat equation describing conductive transport at macroscopic scales, allows studies of CR between arbitrary shapes, thereby generalizing our prior work with slabs [6]. This generalizatin involves compact expressions for the spatially resolved emission and absorption rates throughout the system. However, we show that while there is a general and efficient expression for the spatially resolved RHT rate, a computationally efficient expression for the spatially resolved absorbed power is only feasible when the latter arises from bodies with uniform temperature, which can limit the applicability of the technique to situations involving either small objects or large temperature differentials between objects. As a proof of concept, we consider an idealized, example geometry involving aluminum-zinc oxide (AZO) nanorods separated by vacuum gaps, where one of the nanorods is heated by a large-temperature reservoir while the other is kept at 300K. We show that bulk, nanorod resonances enhance RHT compared to typical surface–plasmon resonances in planar geometries, leading to large and nonlinear temperature gradients.

Coupled radiative and conductive diffusion processes in nanostructures are becoming increasingly important [20], with recent works primarily focusing on the interplay between thermal diffusion and external optical illumination such as laser-heating of plasmonic structures [21–25]. On the other hand, while it is known that conduction has a strong influence on RHT experiments [26], the converse has thus far been largely unexplored because RHT is typically too small to result in appreciable temperature gradients [27–30]. However, our recent work [6] suggests that such an interplay can be significant at tens of nanometer separations and may already be present (though overlooked) in recent experiments [31–34]. Since planar structures are known to exhibit highly suboptimal RHT rates [8], we expect stronger interplay in structured geometries, including recently studied metasurfaces [35], hyperbolic metamaterials [12, 36], and gratings [8, 9, 37].

Formulation.— We first describe a general formulation of coupled CR applicable to arbitrary geometries. Consider a situation involving two bodies (the same framework can be extended to multiple bodies), labelled a and b, subject to arbitrary temperature profiles and exchanging heat among one other, shown schematically in Fig. 1(a). Neglecting convection and considering bodies with lengthscales larger than their phonon mean-free path, in which case Fourier conduction is valid, the stationary temperature distribution satisfies:

$$\nabla \cdot [\kappa(\mathbf{x}) \nabla T(\mathbf{x})] + \int \mathrm{d}^3\mathbf{x}' \, H(\mathbf{x}, \mathbf{x}') = Q(\mathbf{x}) \qquad (1)$$

where $\kappa(\mathbf{x})$ and $Q(\mathbf{x})$ describe the bulk Fourier conductivity and presence of external heat sources at $\mathbf{x}$, respectively, and $H(\mathbf{x}, \mathbf{x}')$ is the radiative power per unit volume from $\mathbf{x}'$ to $\mathbf{x}$.

Our ability to compute $H(\mathbf{x}, \mathbf{x}')$ in full generality hinges on an extension of a recently introduced FVC method that exploits powerful EM scattering techniques [38] to enable

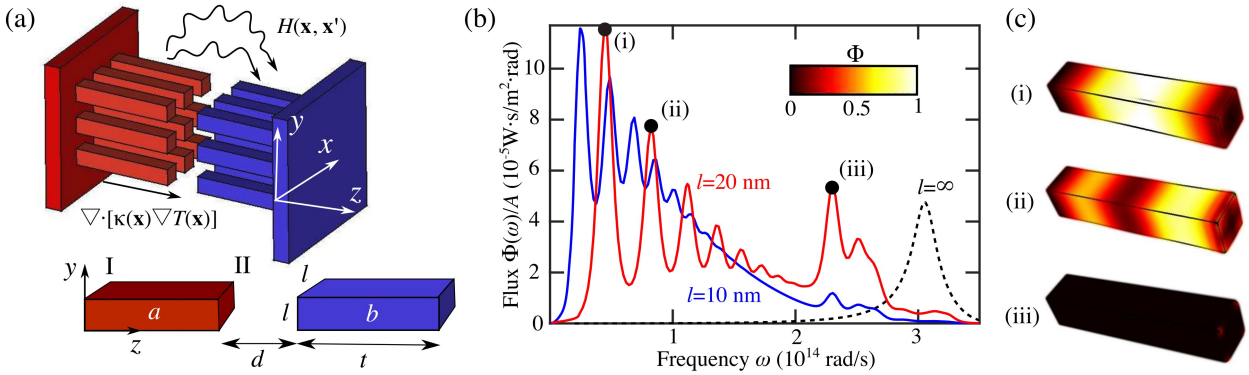

Figure 1. (a) Schematic illustration of two square lattices of nanorods (labelled a and b) of thickness t, period Λ, cross-sectional area $l \times l$, and separation d, whose temperature distribution and energy exchange is mediated by both conductive $\nabla \cdot [\kappa(\mathbf{x}) T(\mathbf{x})]$ and radiative $H(\mathbf{x}, \mathbf{x}')$ heat transfer. (b) Total radiative heat transfer spectrum $\Phi(\omega)$ between two AZO nanorods (solid lines) of thickness $t = 500$ nm and cross-sectional area $A = l^2$, separated by $d = 20$ nm and held at temperatures $T_{a(b)} = 800(300)$ K. The spectrum is shown for different cross-sections $l = \{10, 20\}$ nm (blue and red lines) and in the limit $l = \infty$, corresponding to two planar slabs. (c) Spatial radiative heat flux emitted from nanorod a for the case $l = 20$ nm, corresponding to the (i) first, (ii) second, and (iii) SPP plasmon resonances, respectively, annotated in (b).

fast calculations of RHT under arbitrary geometries and temperature distributions. The starting point of this method is the volume-integral equation (VIE) formulation of EM, in which the scattering unknowns are 6-component polarization currents ξ in the interior of the bodies coupled via the homogeneous 6×6 Green's function Γ of the intervening medium [38]. Given two objects described by a susceptibility tensor $\chi(\mathbf{x})$ and a Galerkin decomposition of the induced currents $\xi = \sum_i y_i b_i$, with $\{b_i\}$ denoting localized basis functions throughout the objects (i is the global index for all bodies), the scattering of an incident field due to some fluctuating current-source $\sigma = \sum_i s_i b_i$ can be determined via solution of a VIE equation, $y + s = Ws$, in terms of the unknown and known expansion coefficients $\{y_i\}$ and $\{s_i\}$, respectively, where $W^{-1}_{i,j} = \langle b_i, (I + i\omega\chi G) b_j \rangle$ and $G_{i,j} = \langle b_i, \Gamma \star b_j \rangle$ are known as VIE and Green matrices [38]. Previously, we exploited this formalism to propose an efficient method for computing the total heat transfer between any two compact bodies [38], based on a simple voxel basis expansion (uniform discretization). The solution of (1) requires an extension of the FVC method to include the spatially resolved heat transfer between any two voxels, which we describe below.

Consider a fluctuating current-source located at $\mathbf{x}_a = b_\alpha$ in body a; such a source induces polarization–currents and EM fields in both objects, with the heat flux at $\mathbf{x}_b = b_\beta$ given by:

$$\Phi(\omega; \mathbf{x}_a \to \mathbf{x}_b) = \frac{1}{2} \langle \mathrm{Re}\left(\xi^*_\beta \phi_\beta\right) \rangle \tag{2}$$

where the subscript β denotes the amplitude of the corresponding quantity at b_β, and "$\langle \ldots \rangle$" the thermodynamic ensemble average. Expressing the polarization–currents and fields in the localized basis $\{b_\alpha\}$, and exploiting the volume equivalence principle to express the field as a convolution of the incident and induced currents with the vacuum Green's function (GF), $\phi = \Gamma \star (\xi + \sigma)$, one finds that (2) can be expressed compactly in terms of the VIE matrices [Supplementary Material (SM)]:

$$\Phi(\omega; \mathbf{x}_a \to \mathbf{x}_b) = \frac{1}{2} \mathrm{Re}\left[D_{\alpha,\alpha} W^\dagger_{\alpha,\beta} (GW)_{\beta,\alpha} \right] \tag{3}$$

where $D_{\alpha,\beta} = \int\int d^3\mathbf{x}\, d^3\mathbf{y}\, b^*_\alpha(\mathbf{x}) \langle \sigma(\mathbf{x}) \sigma^*(\mathbf{y}) \rangle b_\beta(\mathbf{y})$ is a real, diagonal matrix encoding the thermodynamic and dissipative properties of each object [38] and described by the well-known fluctuation–dissipation theorem, $\langle \sigma_i(\mathbf{x}, \omega) \sigma^*_j(\mathbf{y}, \omega) \rangle = \frac{4}{\pi} \omega\, \mathrm{Im}\, \varepsilon(\mathbf{x}, \omega) \Theta(T_\mathbf{x}) \delta(\mathbf{x} - \mathbf{y}) \delta_{ij}$, where $\Theta(T) = \hbar\omega / [\exp(\hbar\omega / k_b T) - 1]$ is the Planck distribution, and $\varepsilon(\mathbf{x}, \omega)$ the dielectric constant at the position $\mathbf{x}$ and frequency ω. Note that we consider situations where the temperature gradient is small compared to the material-dependent current-current correlation lengthscale (of the order of the atomic scale or phonon mean-free path), such that the charge distribution reaches local equilibrium [38, 39]. It follows then that the heat flux emitted or absorbed at $\mathbf{x}_a$, the main quantity entering (1) through $\int \mathrm{d}^3\mathbf{x}'\, H(\mathbf{x}, \mathbf{x}') = \int \mathrm{d}\omega\, \Phi(\omega; \mathbf{x})$, is:

$$\begin{aligned} \Phi(\omega; \mathbf{x}_a) &= \int_{V_b} \mathrm{d}^3\mathbf{x}_b \left[\Phi(\omega; \mathbf{x}_b \to \mathbf{x}_a) - \Phi(\omega; \mathbf{x}_a \to \mathbf{x}_b) \right] \\ &= \frac{1}{2} \mathrm{Tr}_{\,\beta | b_\beta \in V_b} \mathrm{Re}\left[D_{\beta,\beta} W^\dagger_{\beta,\alpha} (GW)_{\alpha,\beta} - (\alpha \leftrightarrow \beta) \right] \\ &= \frac{1}{2} \mathrm{Re}\left[\underbrace{GW D^b W^\dagger}_{\Phi_\mathrm{a}} - \underbrace{D W^\dagger P^b G W}_{\Phi_\mathrm{e}} \right]_{\alpha,\alpha} \end{aligned} \tag{4}$$

Note that here we only integrate over body b because we only consider the impact of externally incident radiation where the temperature differential is largest. To write the matrices and vectors in subspaces spanned by localized basis in each body, we introduce the projection operator $P^{a(b)}$ that selects only basis functions in $a(b)$, such that $D^b = P^b D P^b$ is a diagonal matrix involving only fluctuations in object b (with a more

explicit expression given in [SM] [40]). Furthermore, the first (second) term in (4) describe the absorbed (emitted) power in $\mathbf{x}_a$, henceforth denoted via the subscript "a(e)".

Equation (4) yields the spatially resolved power throughout the entire geometry. In Ref. 38, we showed that the low-rank nature of the GF operator enables truncated, randomized SVD factorizations and therefore efficient evaluations of the corresponding matrix operations, which applies to $\Phi_{\rm e}$ [SM]. We find, however, that in this case, the existence of $\Phi_{\rm a}$ does not permit such a factorization. To understand why, we make use of the detailed balance condition $\Phi(\omega;\mathbf{x}_b \rightarrow \mathbf{x}_a) = \Phi(\omega;\mathbf{x}_a \rightarrow \mathbf{x}_b)$ whenever $T(\mathbf{x}_a) = T(\mathbf{x}_b)$, to obtain an equivalent expression [SM],

$$\Phi_{\rm a}(\omega;\mathbf{x}_a) = \frac{1}{2}\left[\mathrm{Re}(M^{aa}W^{ba\dagger}K^{bb}G^{ba}W^{aa}) + M^{aa}W^{ba\dagger}\,\mathrm{sym}(K^{bb}G^{bb})W^{ba}\right]_{\alpha,\alpha} \tag{5}$$

where $M_{\alpha,\alpha} = \mathrm{Im}\,\varepsilon(\mathbf{x}_\alpha,\omega)$, and $K_{\alpha,\alpha} = D_{\alpha,\alpha}/M_{\alpha,\alpha}$ are real, diagonal matrices encoding only the dissipative properties of the bodies, and the Planck function, respectively, and $X^{ij} = P^i X P^j$ denotes the sub-block of matrix X connecting basis functions in object i to object j. By inspection, one finds that the symmetrized operator in the second term is full rank except whenever the temperature of object b is close to uniform, in which case K^{bb} is nearly diagonal and hence $\mathrm{sym}(K^{bb}G^{bb}) = K^{bb}\,\mathrm{sym}\,G^{bb} + (G^{bb,\dagger}K^{bb} - K^{bb}G^{bb,\dagger})/2 \approx K^{bb}\,\mathrm{sym}\,G^{bb}$. While solution of (5) is in principle feasible, it becomes prohibitive when the number of degrees of freedom is large. It therefore remains an open problem to establish a formulation allowing fast evaluations of the spatially resolved absorbed power under arbitrary temperature distributions.

Given (4), one can solve the coupled CR equation in any number of ways [41]. Here, we exploit a fixed-point iteration procedure based on repeated and independent evaluations of (3) and (1), converging once both quantities approach a set of self-consistent steady-state values. Equation (1) is solved via a commercial, finite-element heat solver whereas (3) is solved through a free, in-house implementation of our FVC method [38]. While the above formulation is general, for computational convenience we consider situations in which object b is kept at a constant, uniform temperature by means of a thermal reservoir, such that the absorbed power in object a can be computed efficiently via (5). The power emitted by a (the heated object), turns out to be much more convenient to compute, since the time-consuming part of the scattering calculation can be precomputed independently from the temperature distribution and stored for repeated and subsequent evaluations of (1) under different temperature profiles.

Results.— As a proof of principle, we consider CR effects in a simple geometry consisting of two metallic nanorods of cross-sectional widths l and thickness t; in practice, to obtain even larger RHT [42], such a structure could be realized as a lattice or grating on a substrate, shown schematically in Fig. 1(a). However, for computational convenience, we restrict calculations to a two-body configuration involving two nanorods separated by a gap, in which only one of the nanorods experiences a large temperature gradient while the other is held at 300K. Such a situation, while highly restrictive, could for instance be realized by requiring large grating periods (in which case multiple-scattering can be safely ignored), low-index substrates (in which case the nanorods are effectively suspended in air), and that one of the nanorods has much higher effective conductivity than the other (e.g. through nanostructuring [43]). The strongest CR effects generally will arise in materials that exhibit large RHT, e.g. supporting surface–plasmon polaritons (SPP), and low thermal conductivities, including silica, sapphire, and AZO, whose typical thermal conductivities $\sim$ 1 W/m·K [44, 45]. In the following, we take AZO as an illustrative example and assume a temperature-independent dielectric constant to illustrate the main effects stemming from CR coupling, leaving a full description, which is more relevant in the presence of large temperature gradients, to future work. Note that we recently considered the full temperature-dependent dielectric response in the context of far-field emission [46, 47], which can also be handled by the FVC framework. To begin with, we show that even in the absence of CR interplay, the RHT spectrum and spatial distribution inside the nanorods differs significantly from those of AZO slabs of the same thickness.

Figure 1(b) shows the RHT spectrum $\Phi(\omega)$ per unit area $A = l^2$ between two AZO nanorods (with doping concentration $11\mathrm{wt}\%$ [45]) of length $t = 500$ nm and varying widths $l = \{10, 20, \infty\}$ nm (blue solid, red solid, and black dashed lines), held at temperatures $T_{a(b)} = 800(300)$ K and vacuum gap $d = 20$ nm. The limit $l \rightarrow \infty$ of a slab–slab geometry was recently studied in Ref. 6, with $\Phi(\omega)$ exhibiting a single peak at the SPP frequency $\approx 3 \times 10^{14}$ rad/s. The finite size of the nanorods leads to additional peaks at lower frequencies, corresponding to bulk plasmon resonances (red and blue solid lines) that provide additional channels of heat exchange, albeit at the expense of weaker SPP peaks, leading to a roughly 5-fold enhancement in RHT compared to slabs. More importantly and well known, such structured antennas provide a mechanism to tune plasmon resonances at near- and far-infrared wavelengths (much lower than many planar materials), which can result in more effective heat exchange. The contour plots in Fig. 1(c) show the spatial RHT distribution $\Phi_{\rm e}(\omega,\mathbf{x})$ (in arbitrary units) at three separate frequencies $\omega = \{0.4, 0.8, 2.3\} \times 10^{14}$ rad/s, corresponding to the first, second, and SPP resonances, respectively. As expected, the largest-frequency resonance is primarily confined to the corners of the nanorods (approaching the slab SPP resonance as $l \rightarrow \infty$), with the lowest-order resonances contributing flux primarily from within the bulk. Such enhancements not only result in larger temperature gradients but also qualitatively change the resulting temperature distributions.

To begin with, we consider a situation in which the boundary I of nanorod a is kept at $T_{\rm I} = 800$ K while the entire nanorod b is held at $T_b = 300$ K. Figure 2(a) shows the temperature profile along the z direction for the $l = d = 20$ nm

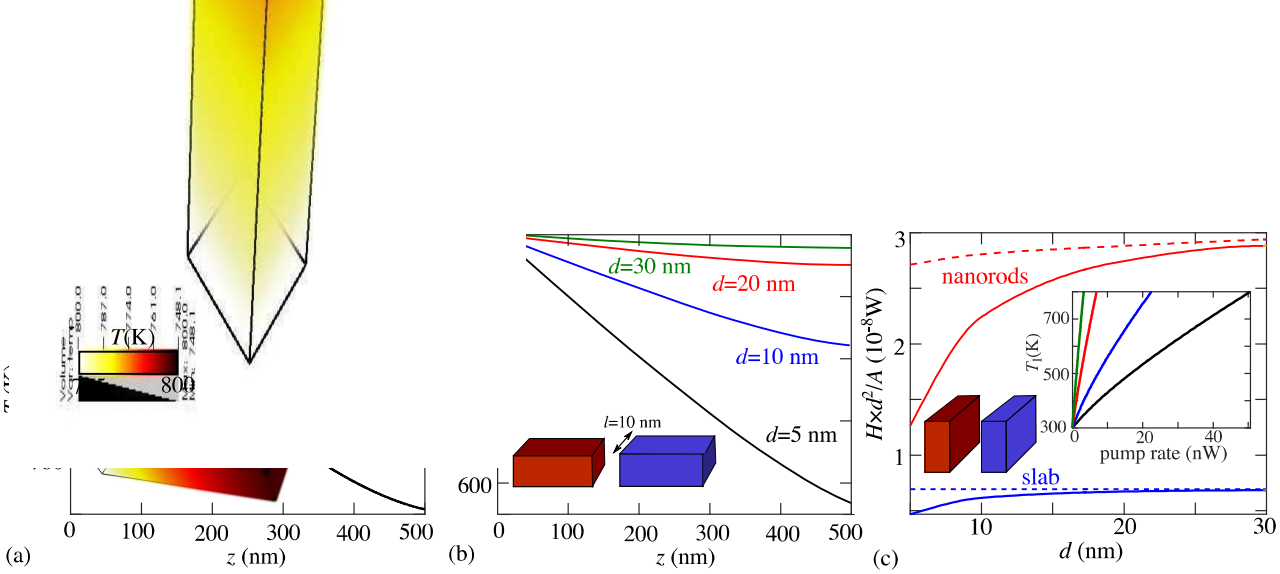

Figure 2. (a) Temperature profile along the z coordinate of a nanorod (solid lines) when it is heated from one side to a temperature of 800 K, and is separated from an identical, constant- and uniform-temperature nanrod held at $T = 300$ K on the other side, by a gap size $d = 20$ nm. The nanorods have cross-sectional width $l = 20$ nm and thicknesses $t = 500$ nm, and are made up of AZO with results shown for multiple values of the doping concentration $\{2, 6, 11\}$wt% (blue, red, and black lines). Also shown are the temperature profiles of slabs (dashed lines) of the same thickness (corresponding to the limit $l \to \infty$). (Inset:) Temperature distribution throughout the nanorod in the case of 11wt%. (b) Temperature profiles of nanorods of width $l = 10$ nm under various separations $d = \{5, 10, 20, 30\}$ nm (black, blue, red, and green lines). (c) The flux value of radiative heat transfer for nanorods (red) and slabs (blue) in the presence (solid lines) or absence (dashed lines) of the temperature gradients induced by the interplay of conduction and radiation. (Inset:) The temperature $T_{\rm I}$ at the interface I of nanorod a as a function of heat pumping rate at I, under various separations $d = \{5, 10, 20, 30\}$ nm (black, blue, red, and green lines).

nanorod geometry of Fig. 1(a), obtained by solving (1) under $Q = 0$. For the sake of generality, we show results under various doping concentrations $\{2, 6, 11\}$wt% (green, red, and black solid lines), resulting primarily in different SPP frequencies [45], and assume an AZO thermal conductivity of $\kappa = 1$ W/m·K [44]. As illustrated for the particular case of 11wt% concentration (inset), the temperature along the x–y cross sections of the nanorods is nearly uniform (due to the faster diffusion rate along this dimension), allowing us to focus on variations along z. In all scenarios, the temperature gradient is significantly larger for nanorods (solid lines) than for slabs ($t \to \infty$, dashed lines), becoming an order of magnitude larger in the case of 6wt% due to the larger SPP frequency, which lies closer to peak Planck wavelength near 800 K. Furthermore, while slabs can only exhibit visible linear temperature profiles in situations involving the largest possible RHT (since RHT here in planar media is dominated by the resonant surface emission [1]), the bulk and de-localized nature of nanorod resonances lead to nonlinear temperature gradients.

Figure 2(b) shows the temperature profile at various separations $d = \{5, 10, 20, 30\}$ nm (black, blue, red, and green lines) and for nanorods of width $l = 10$ nm and doping concentration 11wt%. The figure illustrates the sensitive relationship between CR interplay and gap size. Notably, while RHT and therefore temperature gradients are expected to increase as d decreases, the profile becomes increasingly linear as the geometry approaches the slab–slab configuration. The transition from bulk- to surface-dominated RHT is also evident from Fig. 2(c), which shows the flux rate $H \times d^2$ as a function of d for slabs (black lines) of thickness $t = 500$ nm and nanorods (red lines) of equal thickness and width $l = 10$ nm, in the presence (solid lines) or absence (dashed lines) of CR interplay (with the latter involving uniform temperatures). While RHT between bodies of uniform temperatures scales as $1/d^2$ (dashed lines), the temperature gradients induced by CR interplay in the case of nanorods begins to change the expected powerlaw behavior at $d \approx 20$ nm; the same occurs for slabs but at a shorter $d \lesssim 10$ nm. As shown in Ref. 6, in the limit $d \to 0$, RHT will asymptote to a constant (not shown) rather than diverge. Finally, we also consider the typical and more experimentally relevant scenario of a fixed thermal source of flux rate Q dumping heat evenly at boundary I of nanorod a and thus raising the temperature $T_{\rm I}$ at the interface. Such a pumping mechanism can be implemented through direct laser heating [48], Joule heating [49], or contact with a high-temperature body described by a finite transfer coefficient [30]. The inset of Fig. 2(c) shows $T_{\rm I}$ as a function of Q at multiple $d = \{5, 10, 20, 30\}$ nm (black, blue, red, and green lines), illustrating an decreasing slope $\partial T_{\rm I}/\partial Q$ with decreasing d, with RHT making it harder to maintain higher temperatures. Nevertheless, we find that the previous scenario of a high-temperature boundary $T_{\rm I} = 800$ K requires a moderate heat flux ~ 10 nW at $d = 20$ nm, achievable via recent nanoscale thermal transportation techniques [20].

Concluding remarks.— As experiments continue to push toward larger RHT by going to smaller vacuum gaps or by nanostructuring, accurate descriptions of CR interplay will become increasingly important [19, 20]. In this work, we focused primarily on describing the extension and application of the FVC technique to such situations, providing only a proof-of-concept example where CR interplay is relevant while ignoring other practically important effects associated with the possibility of significant temperature gradients in multiple bodies or additional nonlinearites stemming from the temperature-dependent dielectric response of materials [47].

Future work along these directions could also focus on extending our work to periodic structures, which could potentially exhibit much larger RHT and hence CR effects. Finally, the asymptotic behavior of RHT at short separations is also impacted by surface roughness [50] and ballistic effects (treatable by thermokinetic approaches [27, 51]), making a full description of their combined effects of increasing importance.

Acknowledgements.— This work was supported by the National Science Foundation under Grant no. DMR-1454836 and by the Princeton Center for Complex Materials, a MRSEC supported by NSF Grant DMR 1420541.

[1] S. Basu, Z. Zhang, and C. Fu, International Journal of Energy Research **33**, 1203 (2009).
[2] A. Volokitin and B. N. Persson, Reviews of Modern Physics **79**, 1291 (2007).
[3] R. Ottens, V. Quetschke, S. Wise, A. Alemi, R. Lundock, G. Mueller, D. H. Reitze, D. B. Tanner, and B. F. Whiting, Physical Review Letters **107**, 014301 (2011).
[4] M. T. H. Reid, A. W. Rodriguez, and S. G. Johnson, Proc. IEEE **101**, 531 (2013).
[5] B. Song, A. Fiorino, E. Meyhofer, and P. Reddy, AIP Advances **5**, 053503 (2015).
[6] R. Messina, W. Jin, and A. W. Rodriguez, Physical Review B **94**, 121410(R) (2016).
[7] R. Messina, W. Jin, and A. W. Rodriguez, Physical Review B **94**, 205438 (2016).
[8] O. D. Miller, S. G. Johnson, and A. W. Rodriguez, Physical Review Letters **115**, 204302 (2015).
[9] B. Liu and S. Shen, arXiv preprint arXiv:1509.00939 (2015).
[10] A. D. Phan, L. M. Woods, et al., Journal of Applied Physics **114**, 214306 (2013).
[11] Y. Yang and L. Wang, Physical Review Letters **117**, 044301 (2016).
[12] S.-A. Biehs, M. Tschikin, and P. Ben-Abdallah, Physical review letters **109**, 104301 (2012).
[13] J. Dai, S. A. Dyakov, and M. Yan, Physical Review B **92**, 035419 (2015).
[14] A. W. Rodriguez, M. H. Reid, J. Varela, J. D. Joannopoulos, F. Capasso, and S. G. Johnson, Physical review letters **110**, 014301 (2013).
[15] A. W. Rodriguez, M. H. Reid, and S. G. Johnson, Physical Review B **86**, 220302 (2012).
[16] S. Edalatpour and M. Francoeur, Phys. Rev. B **94**, 045406 (2016).
[17] A. W. Rodriguez, O. Ilic, P. Bermel, I. Celanovic, J. D. Joannopoulos, M. Soljačić, and S. G. Johnson, Physical review letters **107**, 114302 (2011).
[18] K. Joulain, Journal of Quantitative Spectroscopy and Radiative Transfer **109**, 294 (2008).
[19] V. Chiloyan, J. Garg, K. Esfarjani, and G. Chen, Nature Communications **6**, 6775 (2015).
[20] D. G. Cahill, P. V. Braun, G. Chen, D. R. Clarke, S. Fan, K. E. Goodson, P. Keblinski, W. P. King, G. D. Mahan, A. Majumdar, et al., Applied Physics Reviews **1**, 011305 (2014).
[21] G. Baffou, C. Girard, and R. Quidant, Physical review letters **104**, 136805 (2010).
[22] G. Baffou, E. B. Ureña, P. Berto, S. Monneret, R. Quidant, and H. Rigneault, Nanoscale **6**, 8984 (2014).
[23] H. Ma, P. Tian, J. Pello, P. M. Bendix, and L. B. Oddershede, Nano letters **14**, 612 (2014).
[24] C. L. Baldwin, N. W. Bigelow, and D. J. Masiello, The journal of physical chemistry letters **5**, 1347 (2014).
[25] R. Biswas and M. L. Povinelli, ACS Photonics **2**, 1681 (2015).
[26] W. Jin, A. G. Polimeridis, and A. W. Rodriguez, Physical Review B **93**, 121403 (2016).
[27] B. T. Wong, M. Francoeur, and M. P. Mengüç, International Journal of Heat and Mass Transfer **54**, 1825 (2011).
[28] B. T. Wong, M. Francoeur, V. N.-S. Bong, and M. P. Mengüç, Journal of Quantitative Spectroscopy and Radiative Transfer **143**, 46 (2014).
[29] J. Z.-J. Lau, V. N.-S. Bong, and B. T. Wong, Journal of Quantitative Spectroscopy and Radiative Transfer **171**, 39 (2016).
[30] M. Francoeur, R. Vaillon, and M. P. Mengüç, IEEE Transactions on Energy Conversion **26**, 686 (2011).
[31] S. Shen, A. Narayanaswamy, and G. Chen, Nano letters **9**, 2909 (2009).
[32] A. Kittel, W. Müller-Hirsch, J. Parisi, S.-A. Biehs, D. Reddig, and M. Holthaus, Physical review letters **95**, 224301 (2005).
[33] K. Kim, B. Song, V. Fernández-Hurtado, W. Lee, W. Jeong, L. Cui, D. Thompson, J. Feist, M. H. Reid, F. J. García-Vidal, et al., Nature **528**, 387 (2015).
[34] B. Song, Y. Ganjeh, S. Sadat, D. Thompson, A. Fiorino, V. Fernández-Hurtado, J. Feist, F. J. Garcia-Vidal, J. C. Cuevas, P. Reddy, et al., Nature nanotechnology **10**, 253 (2015).
[35] X. Liu and Z. Zhang, ACS Photonics **2**, 1320 (2015).
[36] X. Liu, R. Zhang, and Z. Zhang, International Journal of Heat and Mass Transfer **73**, 389 (2014).
[37] R. Guérout, J. Lussange, F. S. S. Rosa, J.-P. Hugonin, D. A. R. Dalvit, J.-J. Greffet, A. Lambrecht, and S. Reynaud, Phys. Rev. B **85**, 180301 (2012).
[38] A. G. Polimeridis, M. Reid, W. Jin, S. G. Johnson, J. K. White, and A. W. Rodriguez, Physical Review B **92**, 134202 (2015).
[39] A. Perez-Madrid and J. M. Rubi, Phys. Rev. B **77**, 155417 (2008).
[40] See Supplemental Material at [URL] for detailed derivation of the extension for the FVC method.
[41] W. H. Press, *Numerical recipes 3rd edition: The art of scientific computing* (Cambridge university press, 2007).
[42] R. St-Gelais, L. Zhu, S. Fan, and M. Lipson, Nature nanotechnology **11**, 515 (2016).
[43] P. Jood, R. J. Mehta, Y. Zhang, G. Peleckis, X. Wang, R. W. Siegel, T. Borca-Tasciuc, S. X. Dou, and G. Ramanath, Nano letters **11**, 4337 (2011).
[44] J. Loureiro, N. Neves, R. Barros, T. Mateus, R. Santos, S. Filonovich, S. Reparaz, C. M. Sotomayor-Torres, F. Wyczisk, L. Divay, et al., Journal of Materials Chemistry A **2**, 6649 (2014).
[45] G. V. Naik, J. Kim, and A. Boltasseva, Optical Materials Express **1**, 1090 (2011).
[46] W. Jin, A. G. Polimeridis, and A. W. Rodriguez, Phys. Rev. B **93**, 121403 (2016).
[47] E. Blandre, P.-O. Chapuis, and R. Vaillon, Optics express **24**, A374 (2016).
[48] G. Baffou, P. Berto, E. Bermudez Urena, R. Quidant, S. Monneret, J. Polleux, and H. Rigneault, ACS Nano **7**, 6478 (2013).
[49] J. Liang, R. G. D. Jeyasingh, H.-Y. Chen, and H. Wong, Electron Devices, IEEE Transactions on **59**, 1155 (2012).
[50] M. Krüger, V. A. Golyk, G. Bimonte, and M. Kardar, EPL (Europhysics Letters) **104**, 41001 (2013).
[51] A. Pérez-Madrid, L. C. Lapas, and J. M. Rubí, PloS one **8**, e58770 (2013).